Photocatalytic Evidence of the Rutile-to-Anatase Electron Transfer in Titania

Raul Quesada-Cabrera, Carlos Sotelo-Vazquez, Joseph C. Bear, Jawwad A. Darr, and Ivan P. Parkin**

Layered anatase-rutile titania thin-films were synthesized via atmospheric-pressure chemical vapor deposition and characterized using X-ray diffraction, Raman spectroscopy and electron microscopy. The interposition of an amorphous TiO_2-based interlayer allowed direct vapor deposition of anatase on a rutile substrate, which is otherwise hindered by templating. This resourceful approach and the subsequent crystallization of the amorphous layer after annealing of the films allowed investigation on the impact of an efficient interface of the two anatase-rutile phases in the photodegradation of a model organic pollutant. Clear evidence is presented on the synergy between the two polymorphs and more importantly, on the charge flow across the interface, which, against much conventional understanding, it involves electron transfer from rutile to anatase and is in agreement with a recent theoretical model and electron paramagnetic resonance data. Here, an increasing density of trapped electrons on the anatase surface of the A/R film is confirmed by photoreduction of silver. This observation is attributed to a defect-free efficient contact between the two phases and the presence of small rutile particles that promote rapid electron transfer at the A-R interface of the films.

1. Introduction

The synergistic interaction between anatase and rutile TiO_2 polymorphs has been postulated as responsible for the outstanding photocatalytic properties of mixed-phase materials such as the ubiquitous Evonik (formerly Degussa) P25 standard, still a landmark compound as a stable and highly efficient photocatalyst. However, the synergy between anatase and rutile has not been postulated without controversy,[1] particularly concerning the relative position of their corresponding conduction bands. Rutile has been widely regarded as an electron sink in the anatase-rutile system (**Figure 1**(a)). Nevertheless, a recent theoretical model[2] has proposed a staggered band alignment involving electron transfer from rutile to anatase (Figure 1(b)), in agreement with reported electron paramagnetic resonance (EPR) data.[3] To the best of our knowledge, no evidence of the rutile-to-anatase electron transfer has been presented based on standard photocatalytic tests.

In this work, synthesis of bilayer anatase/rutile (A/R) films with effective interface contact was achieved using atmospheric-pressure chemical vapor deposition (APCVD). An inherent issue related to the deposition of an anatase layer on rutile using APCVD is that the latter acts as a template, effectively resulting in a single-phase rutile film. This issue was bypassed here by intercalation of a TiO_2–based layer at relatively low temperature, which essentially produced an amorphous (Am) substrate for the final deposition of the anatase layer. The presence of this Am interlayer in the as-deposited A/Am/R multilayer films and its thermally-induced crystallization, resulting in A/R films, allowed evaluation of an effective interface contact on the photocatalytic activity of these materials during photodegradation of a model organic pollutant (stearic acid). In addition, the photodeposition of silver allowed direct evidence of a drastic increase in electron density on the anatase surface of A/R films, which is consistent with the theoretical and experimental studies reported recently.[2,3]

2. Film Deposition and Characterization

Detailed information on the synthesis of the multilayer films is described in the experimental section. Due to temperature limitation of the CVD rig, a first pure rutile layer was obtained after heat treatment (900 °C, 5 h) of an anatase film deposited on quartz slides. A TiO_2–based non-crystalline (Am) interlayer was then deposited at 300 °C and the subsequent anatase layer was deposited at 500 °C. A side-view scanning electron microscopy (SEM) image of a typical as-prepared A/Am/R film is shown in **Figure 2**(a). Each deposition step was monitored using Raman spectroscopy. The presence of the Am modification was envisaged by significant baseline intensity in the Raman spectrum of the Am/R system (**Figure 3**(b)) compared to that of pure rutile (Figure 3(a)). Further analysis of the Am layer as deposited on

Dr. R. Quesada-Cabrera, C. Sotelo-Vazquez, J. C. Bear, Prof. J. A. Darr, Prof. I. P. Parkin
University College London (UCL)
Dept. Chemistry, Christopher-Ingold Laboratories
20 Gordon St., London WC1H 0AJ, United Kingdom
E-mail: r.quesada@ucl.ac.uk; i.p.parkin@ucl.ac.uk

DOI: 10.1002/admi.201400069

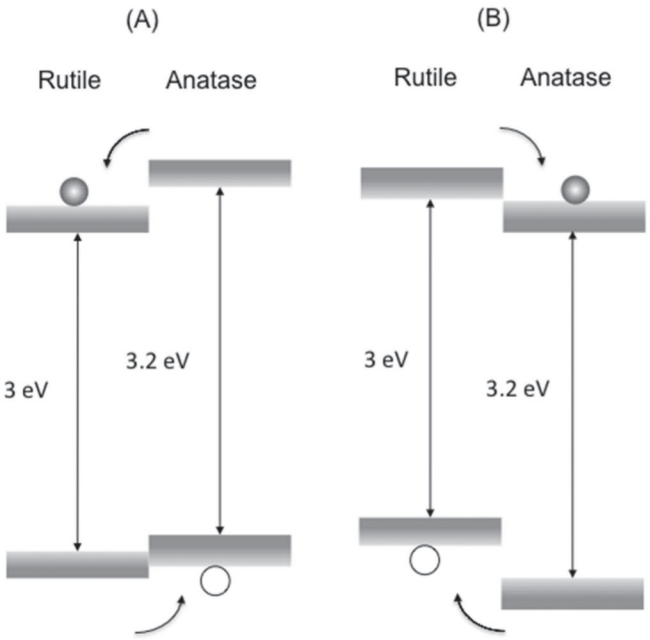

Figure 1. The two models proposed for the relative position of the conduction bands of rutile and anatase TiO_2 polymorphs (adapted from ref. [2]): (A) consensual model denoting rutile as an electron sink; (B) recent configuration proposing electron transfer from rutile to anatase. This work presents evidence that supports model (B).

glass showed broad peaks at *ca.* 150 and 630 cm^{-1}, which are likely related to characteristic E_g modes (144 and 638 cm^{-1}) of the anatase phase. It can be observed that the former band caused broadening of the band at 142 cm^{-1} in the spectrum of rutile (Figure 3(b)). The presence of both crystalline A and R phases was also clearly identified in the Raman studies of multilayer films (Figure 3(d)). It is worth noting that no sign of short-range crystallization of the Am layer, as deposited on glass, was observed under the deposition conditions (500 °C) for at least 1 h, as observed by Raman spectroscopy. Finally, the A/Am/R films were annealed at 500 °C for 10 h in order to induce crystallization of the Am interlayer, resulting in A/R films (Figure 2(b)) with intimate contact.

The presence of both anatase and rutile crystalline polymorphs in the multilayer films was also confirmed using X-ray diffraction (XRD) (**Figure 4**(a)). No traces of any other crystalline phases were identified in any of the films produced in this work. No significant changes were observed in the XRD patterns after annealing of the films (500 °C, 10 h). The latter observations also applied to the control anatase-amorphous A/Am sample (Figure 4(b)) and, as it will be discussed below (*vide infra*), it is implied that the changes estimated in the photoactivities of the films after heat treatment are not merely due to thermally-enhanced crystallinity. Likewise, the heat treatment seemed to promote formation of a defined particulate structure of the films surface (Figure 2(c)), however, it is worth noting that no apparent impact on the photoactivity of the film was attributed to any heat-induced changes in morphology, as evidenced by the photocatalytic behavior of the control anatase-amorphous (A/Am) sample (*vide infra*).

Transmission electron microscopy (TEM) studies on annealed A/R films revealed large areas of highly crystalline material, with interplanar distances $d_A[101] = 3.5$ Å and $d_R[111] = 2.0$ Å assigned to anatase and rutile, respectively (Figure 2(d)). The two polymorphs were also identified by electron diffraction (Figure 2(e)). In the TEM images, anatase and rutile phases seemed to be in intimate contact, which was highlighted by Hurum *et al.*[3] as a condition for an efficient electron transfer from rutile to anatase. These authors also suggested that the presence of atypically small rutile crystallites in small size aggregates (<200 nm) promoted rapid electron transfer between the two polymorphs. The presence of small rutile particles (<100 nm) was clearly identified in this work (Figure 2(f)).

The absorption edge of the pure rutile layer was red-shifted by 40 nm with respect to pure anatase films (**Figure 5**) and their respective bandgap energies were estimated as *ca.* 3 and 3.2 eV, respectively, in agreement with literature values. The absorption spectrum of a typical A/Am/R multilayer film was a combination of the spectra of the isolated crystalline phases and the corresponding bandgap energy was similar to that of rutile (*ca.* 3 eV). In theory, the bandgap energy predicted for a clean anatase-rutile heterojunction (2.78 eV)[2] appears to be red-shifted from those of the pure components. Unfortunately, the high scattering component in the absorption spectra of the annealed A/R films (Figure 5) hindered an accurate estimation of the bandgap energy for comparison with the reported value.

3. Photocatalytic Activity and Synergistic Effect in the A-R Interface

The photoactivity of the films was evaluated during photodegradation of octadecanoic (stearic) acid, a model organic pollutant.[4–8] Stearic acid is highly stable under UV irradiation in the absence of an underlying, effective photocatalyst film. The overall degradation reaction is given by Equation (1) and can be easily monitored for transparent samples *via* infrared spectroscopy, following the disappearance of typical C-H bands at 2958, 2923 and 2853 cm^{-1} (**Figure 6**(a)).

$$CH_3(CH_2)_{16}CO_2H + 26O_2 \xrightarrow{TiO_2 h\nu \geq E_{bg}} 18CO_2 + 18H_2O \quad (1)$$

The number of acid molecules degraded are estimated using a conversion factor from the literature[4] (1 $cm^{-1} \equiv 9.7 \times 10^{15}$ molec. cm^{-2}). The photoactivity rates are estimated from linear regression of the initial 20–30% degradation steps (zero-order kinetics regime) of the curves of integrated areas (Figure 6(b)). These rates are commonly expressed as formal quantum efficiencies (FQE), which estimate the number of acid molecules degraded per incident photon (units, molec. $photon^{-1}$). Any reference to *activity* in this work will be based on FQE results. In the estimation of FQE values, it is considered that all incident photons are absorbed by the photocatalytic films and they all have the same energy, *i.e.* 3.4 eV (365 nm).

The photocatalytic behavior of a range of control and multilayer films was investigated under UVA irradiation (BLB lamp, 1.2 mW cm^{-2}) before and after annealing at 500 °C for 5 and 10 h (**Figure 7**). A thin film of stearic acid was dip-coated onto the anatase surface of the films from a 0.05 M stearic acid solution in chloroform. The original degradation rates followed a

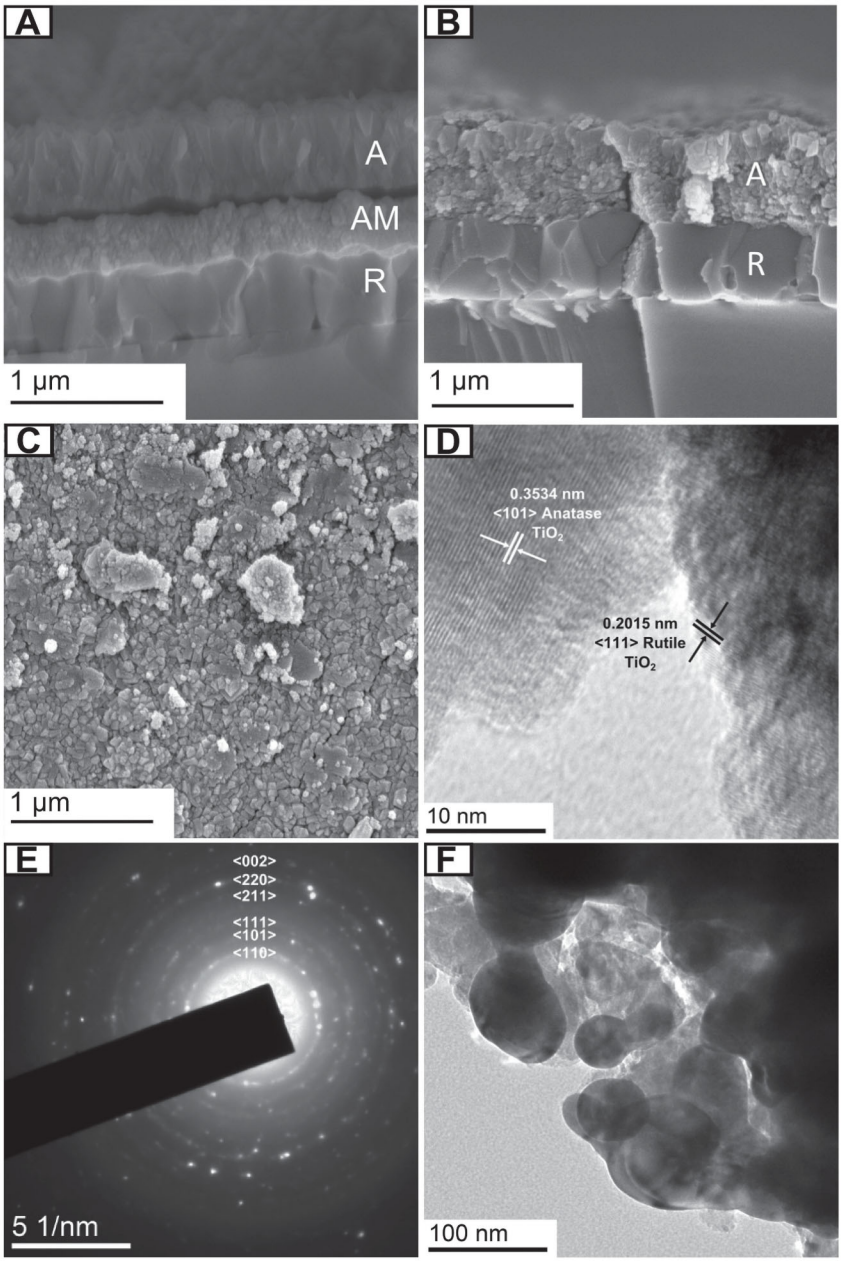

Figure 2. Scanning electron microscopy (SEM) images of (a) as-deposited multilayer A/Am/R film (thickness ~1.5 µm); (b) annealed A/R film (500 °C, 5 h) (thickness ~1.2 µm); (c) anatase surface of a typical A/R film. The transmission electron microscopy (TEM) images show (d) anatase and rutile crystalline phases in the annealed A/R film and corresponding interplanar distances, as indicated ([101] and [111] planes in anatase and rutile, respectively); (e) electron diffraction pattern of rutile; (f) small rutile particles (<100 nm) identified in A/R films.

similar trend to that shown for the corresponding FQE values in Figure 7. The as-deposited A/Am/R multilayer films (samples M1, M2 and M3 in the figure) were designed to contain similar thicknesses of the crystalline phases (A and R), *ca.* 0.5 – 0.6 µm, but different thicknesses of the amorphous Am interlayers (i.e. 0.1, 0.3 and 0.4 µm, respectively). For each individual sample, a boost in activity was always observed after heat treatment at 500 °C for 5 h (samples M1–5T, M2–5T and M3–5T, respectively). This increase in activity could be tentatively attributed to an enhanced overall crystallinity of the films, however, annealing of a control anatase-amorphous film (A/Am, no rutile) at 500 °C for 10 h did not result in the enhancement of the activity (Figure 7) and no major structural changes were observed in the films before and after heat treatment, as evidenced by XRD (Figure 4). Therefore, the increase in activity observed in the case of the multilayer films was attributed to the crystallization of the Am interlayer and hence intimate contact between the two crystalline A/R phases. It was also encouraging to observe that the activities of the annealed samples (M1–5T, M2–5T and M3–5T) did not increase further after a second annealing period (samples M1–10T, M2–10T and M3–10T), which suggests that the crystallization of the Am interlayer was complete over the first 5 h treatment.

The initial activities of the as-deposited A/Am/R films (samples M1, M2 and M3) were significantly higher than those obtained from pure anatase films (samples A1 and A2) of similar thickness (Figure 7). When using APCVD, the formal quantum efficiencies of pure anatase films increase with film thickness within a thickness range below 1 µm.[9,10] However, this trend is not followed using thicker films, which show poor activity (compare samples A1 and A2 in Figure 7). This is probably due to an enhanced charge recombination occurring in the latter case. Therefore, the unexpectedly high activity of the multilayer samples M1, M2 and M3 may be due to the induction of an efficient charge separation and hence a potential contribution of the Am interlayer in the carrier dynamics in these films. This suggestion seems to be supported by correlation between the thickness of the Am interlayer and the activities of samples M1, M2 and M3 (Figure 7). However, this is surprising since it is generally claimed that amorphous TiO_2 induces high charge-carrier recombination [11] and therefore it would be expected for the Am interlayer to hamper electron transfer between the crystalline A,R layers. As expected, the Am layer deposited on glass showed negligible activity in our work (Figure 7). It is worth noting that, as remarked by Ohtani,[12] the results reported for other amorphous TiO_2 samples should not be extended to all non-crystalline TiO_2 modifications that may differ in structure and composition. Indeed, the nature of the Am interlayer in the A/Am/R system may differ from that of the amorphous Am layer as deposited on glass, shown in Figure 3(c). The former may be a highly distorted modification of either anatase or rutile structures and its potential role in the charge transfer between the crystalline A,R phases is not known. In fact, the existence

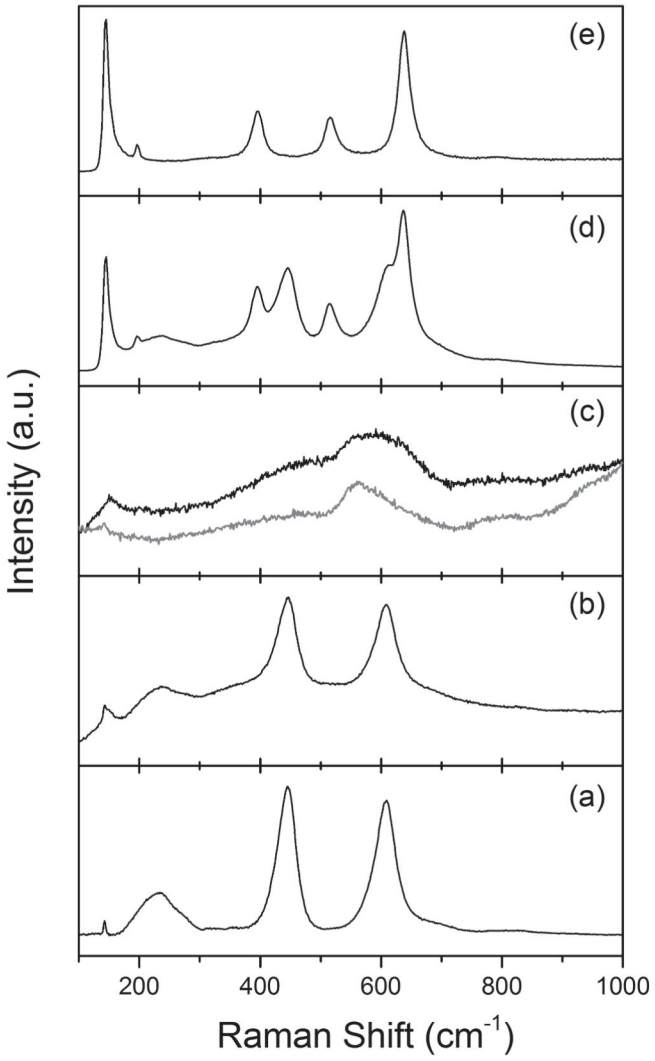

Figure 3. Raman spectra of (a) rutile (R) on quartz; (b) amorphous Am layer as deposited on rutile (Am/R); (c) amorphous Am layer on plain glass (black line) and corresponding spectrum of the glass substrate (grey line); (d) typical A/R film; (e) pure anatase film on glass.

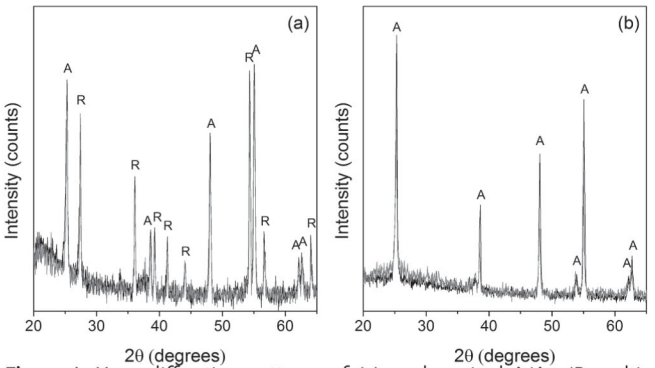

Figure 4. X-ray diffraction patterns of (a) as-deposited A/Am/R multilayer film and (b) control A/Am film (black lines). The grey lines show XRD patterns of the corresponding films (A/R and A, respectively) after heat treatment at 500 °C for 10 h.

of a highly distorted interface between anatase and rutile has been suggested in the literature.[3,13,14] Also highly distorted regions in the A/R system have been proposed as rutile nucleation sites that favor the rapid electron transfer between the two polymorphs.

The significant increase in photocatalytic activity when comparing samples before and after annealing validates the synergistic interaction between the TiO_2 crystalline polymorphs. Nonetheless, this condition is *necessary* but not *sufficient* in the argument of electron transfer in the A/R system. Hydroxyl and hydroperoxyl radicals (•OH, $•O_2H$) as well as oxo species ($•O_2^-$, $^1O_2$) formed by photogenerated holes and electrons, respectively, are proposed to participate in the degradation of organic compounds.[12,15]

Insight on the direction of charge carrier flows may be obtained following the deposition of silver (Ag) metal particles upon reduction of Ag^+ ions by photogenerated electrons trapped on the surface of the photocatalyst.[16,17] Rutile and anatase show different ability to photoreduce Ag^+ ions. A high concentration of small Ag particles typically coats the surface of rutile (**Figure 8**(a)) whilst large Ag aggregates are usually observed on the anatase phase (Figure 8(b)). The latter observation is indicative of active sites (*hot spots*) involving accumulation of photogenerated electrons trapped on the anatase surface.[18] Here, selected films were coated simultaneously under solar simulator irradiation conditions (75 W Xe lamp, Am 1.5 air mass filter) in 40 ml of aqueous silver nitrate solution (0.5 M $AgNO_3$) under strong stirring conditions (2.5 h). The solution was purged with argon during 30 min prior to illumination. The presence of Ag metal particles was confirmed by elemental analysis (EDX) and monitored *via* back-scattered SEM images (Figure 8). As expected, scattered lumps of Ag metal were found in a pure anatase film (initially A/Am but annealed at 500 °C for 10 h) (Figure 8(b). Similar aggregates were still observed on the anatase surface of the multilayer A/Am/R film before annealing (Figure 8(c)); however, a high concentration of Ag particles coated the whole surface, suggesting an increase in the density of photogenerated electrons. This observation is consistent with the increase in activity of the as-deposited A/Am/R multilayer films compared to that of pure anatase during the photodegradation of stearic acid (Figure 6). Notably, a drastic increase in the density of Ag metal deposits was observed on the annealed A/R film (Figure 8(d)), which is attributed to an effective contact between the crystalline polymorphs. These Ag deposits were presented as needles and large aggregates and they are presumably the result of alternating electronic and ionic events, commonly described by Equation (2).[17,19] The latter observation clearly shows the electron transfer occurring from rutile to anatase.

$$Ag^0 + Ag^+ \rightarrow (Ag)_2^+ \xrightarrow{e-} Ag_2 \xrightarrow{Ag^+} (Ag)_3^+ \xrightarrow{e-} Ag_3 \rightarrow \ldots \rightarrow Ag_m \quad (2)$$

Interestingly, Kawahara *et al.*[20] reported SEM results of silver deposition on anatase-rutile patterned films, as synthesized from sol-gel anatase stripes on sputtered rutile substrates (both phases exposed to the testing media). In that work, large Ag particles were observed on the anatase surface and a cloud

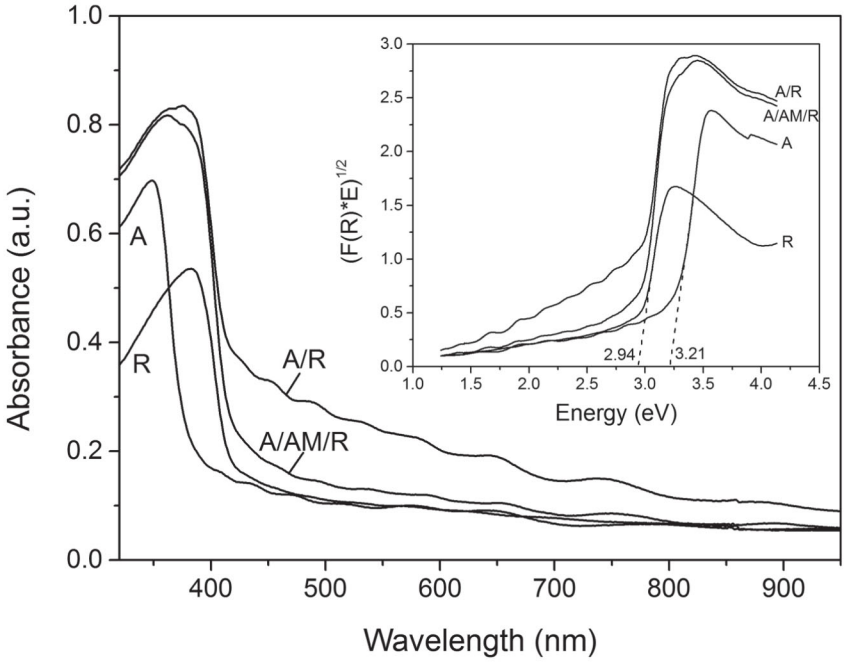

Figure 5. Absorption spectra of anatase (A), rutile (R) and multilayer films before (A/Am/R) and after (A/R) heat treatment at 500 °C for 10 h. Inset: Tauc plots showing approximate bandgap energy values of the A,R crystalline phases.

of small Ag particles on the rutile side of the boundary region. The authors noticed the apparent inactivity of rutile, which was attributed to possible structure insensitivity of the [110] crystal plane of the sputtered rutile phase. Close inspection of the cloud of Ag particles on the rutile phase showed an increase in particle size towards the A-R junction. Based on the scale of the diffusion length of electrons in solids, estimated as being of the same order (5.1 µm) than the extent of the Ag cloud on the rutile side, the authors concluded that electrons flowed from anatase to rutile. These observations may be related to deep trapping sites that would reverse the predicted electron transfer direction. However, assuming that the sol-gel anatase phase forms a defect-free buried heterojunction with the rutile substrate, the increasing growth rate of Ag particles observed in their SEM images could also be explained by an increasing density of electrons towards the rutile-anatase boundary, where a *tail* rather than a *cloud* of particles may be expected. Thus, the results reported by Kawahara *et al.*[20] could also support the recent theoretical model and correlate with our observations.

4. Conclusion

Anatase-rutile TiO_2 layered films were prepared by atmospheric-pressure chemical vapor deposition and the synergistic interaction between these polymorphs demonstrated during photodegradation of stearic acid and photodeposition of silver. The traditional impediment where rutile acts as a template for the subsequent deposition of an anatase layer using APCVD was surpassed here by intercalation of a non-crystalline TiO_2-based layer and additional heat-treatment of the films at 500 °C for several hours. The resulting A/R films showed specific properties that have been identified as essential for an efficient electron transfer from rutile to anatase, such as an atypical size of rutile particles. A boost in photocatalytic activity after the annealing of multilayer films, which was not detected in the case of control anatase samples, was explained in terms of an efficient contact between the two crystalline polymorphs. Further comparison in the behavior of multilayer films and the pure crystalline phases during photodeposition of silver particles allowed conclusions on the directional flow of photogenerated electrons to be drawn.

The results presented here are the first rutile-to-anatase evidence based on simple photocatalytic tests, to the best of our knowledge. This work highlights the importance of

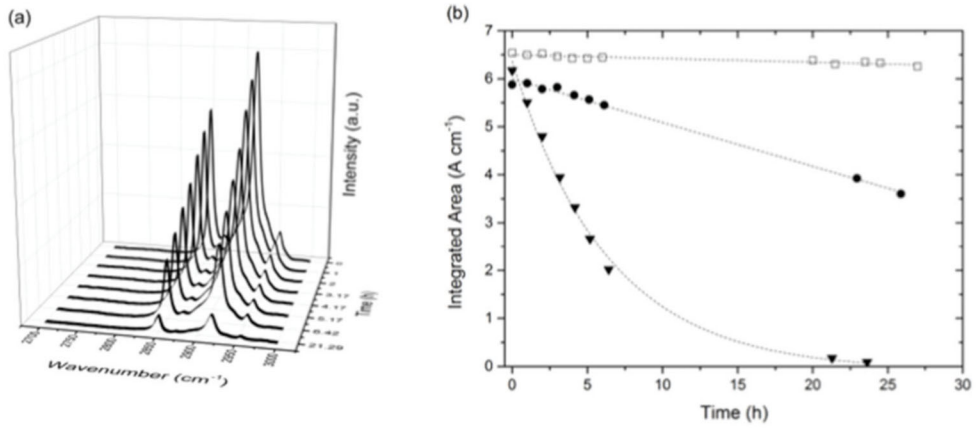

Figure 6. (a) IR spectra of stearic acid upon UVA illumination (1.2 mW cm^{-2}) on a typical A/R film. (b) Integrated areas obtained during illumination of A/R (full triangles) and control A/Am (full circles) films. A blank test corresponding to stearic acid on plain glass is included for reference (empty symbols).

ADVANCED MATERIALS INTERFACES
www.advmatinterfaces.de

Materials Views
www.MaterialsViews.com

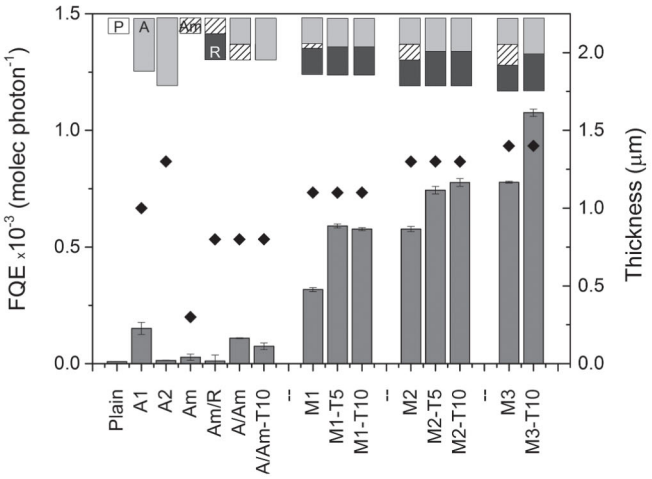

Figure 7. Formal quantum efficiencies, given as molecules degraded per incident photon (molec. photon^{-1}), obtained from the initial rates of photodegradation of stearic acid under UVA illumination (1.2 mW cm^{-2}). Three different as-deposited A/Am/R multilayer films (M1, M2, M3) are included, containing similar thicknesses of crystalline A,R layers (0.5 – 0.6 μm) but different thicknesses of amorphous interlayers (0.1, 0.3 and 0.4 μm, respectively, as indicated). Full diamonds represent the approximate total thickness of the films. Schematic representations of the layer structures are included for guidance. Light grey frames are anatase (A), dark grey frames are rutile (R) and patterned frames represent the amorphous interlayer (Am). The frames in these representations are scaled according to the approximate thickness of the corresponding layers. The annealing times 5 and 10 h at 500 °C are indicated as T5 and T10, respectively. The activities of pure anatase films of different thickness (A1, A2) have been included as reference. The thickness of A1 was identified as the optimum thickness (~1 μm) for pure anatase films in this work, based on FQE values. A control A/Am film formed by anatase and amorphous layers only (no rutile), and amorphous layers as deposited on glass (Am) and rutile (Am/R) are included for reference, as well as the apparent degradation of stearic acid on plain glass (P).

establishing controlled conditions in the design of a next generation of photocatalysts, aiming for adequate interface contact and physical properties such as particle size, morphology and crystallinity of these materials.

5. Experimental Section

Film synthesis: Titanium tetrachloride ($TiCl_4$, 99%) and ethyl acetate ($C_4H_8O_2$, 99.8%), both from *Sigma-Aldrich*, were used as metal and oxygen sources, respectively.[21] The precursors were heated independently in stainless steel bubblers and carried under controlled flows using pre-heated nitrogen gas (200 °C; *BOC*). The precursors were mixed in a mixing chamber (250 °C) before accessing the CVD reactor. The cold-wall CVD reactor consisted of a quartz tube containing a 320 mm-long graphite block with three inserted Whatman heater cartridges. The temperature of the entire system was controlled by Pt-Rh thermocouples. In a typical deposition, bubbler temperatures and gas flows of the precursors were set to 1.2 L min^{-1}/70 °C and 0.25 L min^{-1}/40 °C for $TiCl_4$ and $C_4H_8O_2$, respectively. The first TiO_2 layer was deposited (growth rate, 0.25 – 0.3 μm min^{-1}) on quartz slides (25×25 mm, *Multi-Lab*) at 500 °C and then annealed to 900 °C for 5 h. X-ray diffraction and Raman spectroscopy confirmed the presence of pure rutile; no traces of anatase were detected. A second layer (Am phase) was deposited at 300 °C allowing different deposition times (0.1 μm min^{-1}). Finally, a third TiO_2 layer (0.25 – 0.3 μm min^{-1}), which

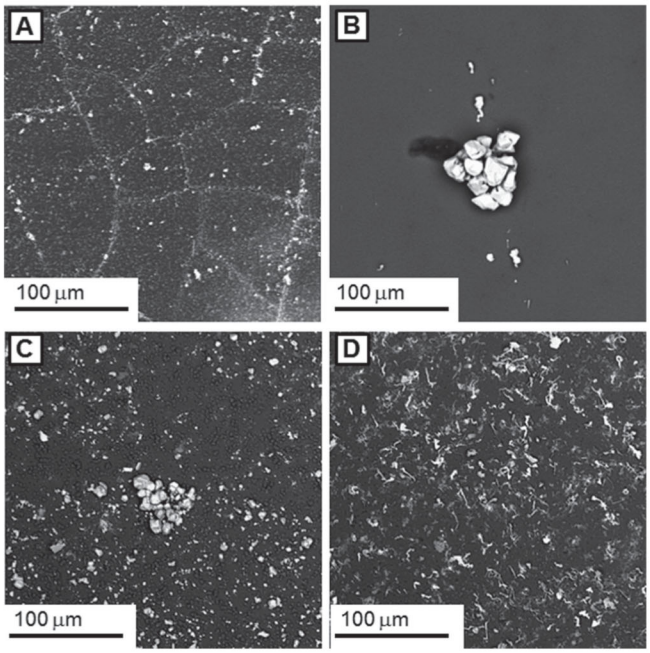

Figure 8. Backscattered SEM images of selected films (20 kV, x300) after photodeposition of Ag particles. (A) Rutile; (B) Anatase; (C) as-deposited multilayer A/Am/R film; (D) annealed multilayer A/R film (500 °C, 10 h). The presence of Ag particles (light grey) is clearly highlighted against the TiO_2 background (dark grey). The composition of the films was also checked by elemental analysis (EDX).

was confirmed to be pure anatase, was deposited at 500 °C. Heat treatment of the films was then carried out at 500 °C for 5 and 10 h. The quartz slides were only kept in the reactor during the actual deposition time of the Am interlayer (a few minutes) and the anatase phase (2 min) in order to avoid the potential crystallization of the Am layer.

Film characterization: X-ray diffraction (XRD) studies were carried out using a Bruker-Axs D8 (GADDS) diffractometer. The instrument operates with a Cu X-ray source, monochromated ($K\alpha_1$ and $K\alpha_2$) and a 2D area X-ray detector with a resolution of 0.01° (glancing incident angle, θ = 5°). The diffraction patterns obtained were compared with database standards. Raman spectroscopy was carried out using a Renishaw 1000 spectrometer equipped with a 633 nm laser. The Raman system was calibrated using a silicon reference. UV/vis spectroscopy was performed using a Perkin Elmer Lambda 950 UV/Vis/NIR Spectrophotometer. The absorption spectra were recorded directly on the films as deposited on quartz slides, clamped against the integrating sphere in perpendicular position to the beam path. A Labsphere reflectance standard was used as reference in the UV/vis measurements. Scanning electron microscopy (SEM) and energy-dispersive X-ray spectroscopy (EDX) were carried out using a Jeol JSM-6700F and secondary electron image on a Hitachi S-3400N field emission instruments (20 KV) and the Oxford software INCA. X-Ray photoelectron spectroscopy (XPS) was performed using a Thermo Scientific K-alpha spectrometer with monochromated Al Kα radiation, a dual beam charge compensation system and constant pass energy of 50 eV (spot size 400 μm). Survey scans were collected in the range 0–1200 eV. High-resolution peaks were used for the principal peaks of Ti (2p), O (1s), N (1s), C (1s) and Si (2p). The peaks were modelled using sensitivity factors to calculate the film composition. The XPS data indicated at.% Ti:O ratios of *ca*. 1:2 for all our films. Transmission electron microscopy (TEM) images and selected area electron diffractograms (SAEDs) were obtained using a high resolution TEM Jeol 2100 with a LaB_6 source operating at an acceleration voltage of 200 kV. Micrographs were recorded on a Gatan Orius Charge-coupled device (CCD). The films were scrapped off the quartz substrate using a diamond pen, sonicated

and suspended in chloroform and drop-casted onto a 400 Cu mesh lacy carbon film grid (Agar Scientific Ltd.) for TEM analysis.

Photocatalytic test and irradiation sources: A Perkin Elmer RX-I Fourier transform infrared (FTIR) spectrometer was used to monitor the degradation of stearic acid in the photocatalytic tests. Blacklight-blue (BLB) lamps (365 nm, 2 × 8 W, 1.2 mW cm^{-2}) were used in the stearic acid tests and a 75 W Xe lamp source, provided with an AM1.5 air mass filter (solar simulator), was used for the photodeposition of silver. The irradiance of the BLB lamp was measured using a UVX radiometer (from UVP). The emission spectra of the light sources were recorded using a *Ocean Optics* spectrometer. The spectrum from the BLB lamp showed a relatively wide band (FWHM ~25 nm) centered at 365 nm.

Acknowledgements

Kevin Reeves and Steven Firth are thanked for allowing access to the SEM and TEM instruments. This work was funded by the PCATDES Consortium grant, Seventh Framework Programme (N. 309846).

Received: January 30, 2014
Revised: March 21, 2014
Published online: April 16, 2014

[1] a) G. Li, K. A. Gray, *Chem. Phys.* **2007**, *339*, 173; b) S. G. Kumar, L. G. Devi, *J. Phys. Chem. A* **2011**, *115*, 13211.
[2] D. O. Scanlon, C. W. Dunnill, J. Buckeridge, S. A. Shevlin, A. J. Logsdail, S. M. Woodley, C. R. A. Catlow, M. J. Powell, R. G. Palgrave, I. P. Parkin, G. W. Watson, T. W. Keal, P. Sherwood, A. Walsh, A. A. Sokol, *Nat. Mater.* **2013**, *12*, 798.
[3] D. C. Hurum, A. G. Agrios, K. A. Gray, T. Rajh, M. C. Thurnauer, *J. Phys. Chem. B* **2003**, *107*, 4545.
[4] A. Mills, J. S. Wang, *J. Photochem. Photobiol. A Chem.* **2006**, *182*, 181.
[5] Y. Paz, Z. Luo, L. Rabenberg, A. Heller, *J. Mater. Res.* **1995**, *10*, 2842.
[6] D. Ollis, *Appl. Cat. B Environ.* **2010**, *99*, 478.
[7] P. Sawunyama, A. Fujishima, K. Hashimoto, *Langmuir* **1999**, *15*, 3551.
[8] J. T. Remillard, J. R. McBride, K. E. Nietering, A. R. Drews, X. Zhang, *J. Phys. Chem. B* **2000**, *104*, 4440.
[9] A. Kafizas, C. J. Carmalt, I. P. Parkin, *Chem. Eur. J.* **2012**, *18*, 13048.
[10] G. Hyett, M. Green, I. P. Parkin, *J. Am. Chem. Soc.* **2006**, *128*, 12147.
[11] B. Ohtani, Y. Ogawa, S-I. Nishimoto, *J. Phys. Chem. B* **1997**, *101*, 3746.
[12] B. Ohtani, *Chem. Lett.* **2008**, *37*, 217.
[13] N. A. Deskins, S. Kerisit, K. M. Rosso, M. Dupuis, *J. Phys. Chem. C* **2007**, *111*, 9290.
[14] R. L. Penn, J. F. Banfield, *Am. Miner.* **1999**, *84*, 871.
[15] M. R. Hoffmann, S. T. Martin, W. Choi, D. W. Bahnemann, *Chem. Rev.* **1995**, *95*, 69.
[16] T. Torimoto, N. Nakamura, S. Ikeda, B. Ohtani, *Phys. Chem. Chem. Phys.* **2002**, *4*, 5910.
[17] H. H. Mohammed, D. W. Bahnemann, *Appl. Catal. B Environ.* **2012**, *128*, 91.
[18] W. E. Farneth, R. S. McLean, J. D. Bolt, E. Dokou, M. A. Barteau, *Langmuir* **1999**, *15*, 8569.
[19] M. D. Ward, A. J. Bard, *J. Phys Chem.* **1982**, *86*, 3599.
[20] T. Kawahara, Y. Konishi, H. Tada, N. Tohge, J. Nishii, S. Ito, *Angew. Chem.* **2002**, *114*, 2935.
[21] S. A. O'Neill, I. P. Parkin, R. J. H. Clark, A. Mills, N. Elliott, *J. Mater. Chem.* **2003**, *13*, 56.

